

SPECTRAL ENERGY DISTRIBUTIONS OF WEAK ACTIVE GALACTIC NUCLEI ASSOCIATED WITH LOW-IONIZATION NUCLEAR EMISSION REGIONS

MICHAEL ERACLEOUS^{1,2,3}, JASON A. HWANG^{1,3}, & HÉLÈNE M. L. G. FLOHIC^{1,4}

To Appear in the *Astrophysical Journal Supplements*

ABSTRACT

We present a compilation of spectral energy distributions (SEDs) of 35 weak active galactic nuclei (AGNs) in low-ionization nuclear emission region (LINERs) using recent data from the published literature. We make use of previously published compilations of data, after complementing and extending them with more recent data. The main improvement in the recent data is afforded by high-spatial resolution observations with the *Chandra X-Ray Observatory* and high-spatial resolution radio observations utilizing a number of facilities. In addition, a considerable number of objects have been observed with the *Hubble Space Telescope* in the near-IR through near-UV bands since the earlier compilations were published. The data include upper limits resulting from either non-detections or observations at low spatial resolution that do not isolate the AGN. For the sake of completeness, we also compute and present a number of quantities from the data, such as optical-to-X-ray spectral indices (α_{ox}), bolometric corrections, bolometric luminosities, Eddington ratios, and the average SED. We anticipate that these data will be useful for a number of applications. In a companion paper, we use a subset of these data ourselves to assess the energy budgets of LINERs.

Subject headings: galaxies: nuclei — galaxies: active — X-rays: galaxies

1. INTRODUCTION

Low-ionization nuclear emission regions (LINERs) were identified as a class by Heckman (1980) based on the relative intensities of their oxygen emission lines. Their defining properties are: $[\text{O II}] \lambda 3727 / [\text{O III}] \lambda 5007 > 1$ and $[\text{O I}] \lambda 6300 / [\text{O III}] \lambda 5007 > 1/3$. Optical spectroscopic surveys (e.g., Ho, Filippenko, & Sargent 1997a) have shown them to be very common, occurring in approximately 50% of the nuclei of nearby galaxies. Suggestions for the ultimate power source of the emission lines include (a) a weak active galactic nucleus (an AGN harboring an accreting, supermassive black hole; e.g. Halpern & Steiner 1983; Ferland & Netzer 1983), (b) hot stars (either young or old, e.g. Terlevich & Melnick 1985; Filippenko & Terlevich 1992; Shields 1992; Barth & Shields 2000; Binette et al. 1994), and (c) shocks (e.g. Heckman 1980; Dopita et al. 1996, and references therein). Recent radio, UV, and X-ray surveys at high spatial resolution, mid-IR spectroscopy, and variability studies have uncovered weak AGNs in the majority of LINERs studied so far, suggesting that they make up a large (perhaps the largest) subset of all AGNs (e.g. Filho et al. et al. 2004; Nagar, Falcke, & Wilson 2005; Barth et al. 1998; Maoz et al. 2005; Ho et al. 2001; Terashima & Wilson 2003; Dudik et al. 2005; Flohic et al. et al. 2006; González-Martín et al. 2006; Dudik, Satyapal, & Marcu 2009)

The ubiquity of LINERs suggests that they are an important component of the nuclei of galaxies in the local universe. Moreover, they trace the population of AGNs at the lowest luminosities. The data available from the most modern observing facilities allow us to address a number of outstand-

ing questions related to LINERs and their central engines, such as whether the weak AGNs are responsible for powering the emission-line regions by photoionization, whether or not models for low-radiative efficiency accretion flows provide a good description of the properties of these weak AGNs, and what is the role of feedback of the weak AGN on the central region of its host galaxy (see the discussion of these and other related issues in Ho 2008). A good example of such an application is the work of Maoz (2007), who independently collected measurements at very specific frequencies for a subset of the objects in our sample.

Motivated by the above questions we set out to collect published data from the recent literature to define the spectral energy distributions (SEDs) of weak AGNs in LINERs at photon energies above 1 Ry. Our primary interest was to assess the energy budgets of LINERs and investigate whether the AGN is powerful enough to power the the observed emission lines by photoionization. In the process we constructed the full SEDs (from radio to X-ray energies), thus extending and updating the pioneering work of Ho (1999). In this paper we present the data and a number of quantities derived from them without any scientific interpretation. We anticipate that this compilation of data will be useful for a number of additional applications, including those mentioned in the previous paragraph. In a followup paper we use a subset of the data presented here to address the specific question regarding the energy budget of LINERs (Eracleous et al. 2009, hereafter paper II).

In §2 we present the sample of galaxies and their basic properties. In §3 we present the SEDs, discuss extinction corrections, and comment on a number of objects that warrant special attention. Finally, in §4 we present a number of quantities derived from the data, namely the optical-to-X-ray spectral indices (α_{ox}), the bolometric luminosities, Eddington ratios, and the average SED. We provide details of how we selected the data and how we converted the measured quantities to “monochromatic” luminosities. We emphasize caveats and sources of uncertainty in our methods. We also catalog the

¹ Department of Astronomy and Astrophysics, The Pennsylvania State University, 525 Davey Lab, University Park, PA 16802

² Center for Gravitational Wave Physics, The Pennsylvania State University, 104 Davey Lab, University Park, PA 16802

³ Department of Physics & Astronomy, Northwestern University, 2131 Tech Drive, Evanston, IL 60208

⁴ Department of Physics and Astronomy, University of California, 4129 Frederick Reines Hall, Irvine, CA 92697

original data (with appropriate references to the source of the information) so that one can reproduce our procedures with modifications, if desired.

2. TARGETS AND THEIR PROPERTIES

We constructed a sample of objects classified as LINERs or transition objects by Ho et al. (1997b)⁵ based on the following considerations. All objects were required to have measured optical emission line luminosities and X-ray observations with *Chandra* that yielded a measurement of the AGN X-ray spectrum or an upper limit to its X-ray flux. The high spatial resolution of *Chandra* allows us to spatially separate the AGN emission from most of the diffuse, thermal X-ray emission. We showed preference to objects observed in the X-ray band with long exposure times i.e., objects whose X-ray spectra have high signal-to-noise ratio (S/N). In such cases, a model fit to the AGN spectrum can give a direct estimate of the total extinction toward the AGN continuum source. Moreover, any soft, unresolved, circumnuclear X-ray emission can be separated spectrally. A significant subset of the sample objects were imaged in the UV with the *HST* and an overlapping subset had well sampled SEDs in the entire range from the radio to X-ray bands. We took advantage of these overlapping subsets in order to determine upper limits to the UV fluxes when they were not measured directly and to determine bolometric luminosities from the data, as we detail in §3.

We relied heavily on previously published compilations of data (e.g., Ho 1999; Ptak et al. 2004) and on papers presenting large collections of measurements in the radio, UV, or X-ray bands (e.g., Nagar et al. 2005; Doi et al. 2005b; Maoz et al. 2005; Flohic et al. et al. 2006). We note that the work of Maoz et al. (2005) is particularly important because it uses variability in the UV continuum to check whether the nuclear source in a LINER is an AGN. The previously published compilations were updated and supplemented with data that became available later. Because of possible contamination of the AGN emission by circumnuclear emission, we adopted measurements from high-spatial resolution observations which isolate the AGN. In the near-IR, optical, and near-UV bands, when given a choice we adopted measurements from images rather than from spectra. The high spatial resolution of *Chandra* and the *HST* were optimal (see example images in Eracleous et al. 2002; Flohic et al. et al. 2006). In the radio band, possible confusion from circumnuclear emission (or in some cases jets) is also possible, therefore we relied on high-resolution VLA or VLBA/VLBI observations. For the sake of completeness, we also include measurements made at low spatial resolution, but we take these as upper limits to the flux of the AGN. Included in the sample are 13 LINERs with actual X-ray and UV (2500 Å) measurements, 11 LINERs with actual X-ray measurements but no UV measurements, 6 LINERs with actual UV (2500 Å) measurements and X-ray upper limits, and 5 LINERs with X-ray upper limits only.

The galaxies of the resulting sample are listed in Table 1 along with their morphological types and distances. Table 2 lists Galactic reddening, central stellar velocity dispersion and inferred black hole mass, and LINER type for the nuclei of the sample galaxies. The Galactic reddening was taken from Schlegel et al. (1998). In Figure 1 we show the distributions of the distances reported by Tully (1988), the morphological

⁵ Hereafter, we refer to all objects collectively as “LINERs.” In §2.2 we re-examine their classifications based on more recently developed criteria and conclude that they can all be regarded as LINERs.

TABLE 1
SAMPLE OF GALAXIES AND THEIR BASIC PROPERTIES

| Galaxy (1) | Hubble Type ^a (2) | Distance (Mpc) | | | |
|--------------------------|------------------------------------|---------------------------|-------------------------|--------------------------|---------------------------|
| | | Tully ^b (3) | SBF ^c (4) | PNLF ^d (5) | Other ^e (6) |
| NGC 0266 | SB(rs)ab | 62.4 | | | |
| NGC 0404 | SA(s)0 | 2.4 | 3.0 | | 3.1 |
| NGC 1097 | SB(rl)b | 14.5 | | | |
| NGC 1553 | SA(rl)0 | 13.4 | 17.2 | | |
| NGC 2681 | SBA(rs)0/a | 13.3 | 16.0 | | |
| NGC 3031 (M81) | SA(s)ab | 3.6 | 3.6 | | 3.6 |
| NGC 3169 | SA(s)a | 19.7 | | | |
| NGC 3226 | E2 | 23.4 | 21.9 | | |
| NGC 3379 (M105) | E1 | 8.1 | 9.8 | 10.4 | |
| NGC 3507 | SB(s)b | 19.8 | | | |
| NGC 3607 | Sa(s)0 | 19.9 | 21.2 | | |
| NGC 3608 | E2 | 23.4 | 21.3 | | |
| NGC 3628 | SAb | 7.7 | | | |
| NGC 3998 | SA(r)0 | 14.0 | 13.1 | | |
| NGC 4111 | SA(r)0 | 17.0 | 13.9 | | |
| NGC 4125 | E6 | 24.2 | 22.2 | | |
| NGC 4143 | SAB(s)0 | 17.0 | 14.8 | | |
| NGC 4261 (3C 270) | E2-3 | 30.0 | 31.6 | | 36.1 |
| NGC 4278 | E1-2 | 9.7 | 14.9 | | |
| NGC 4314 | SB(rs)a | 9.7 | | | |
| NGC 4374 (M84, 3C 272.1) | E1 | 16.8 | 17.1 | 18.0 | |
| NGC 4438 | SA(s)0/a | 16.8 | | | 11.3 |
| NGC 4457 | SAB(s)0/a | 17.4 | | | 10.7 |
| NGC 4486 (M87, 3C 274) | E0-1 | 16.8 | 14.9 | 15.8 | |
| NGC 4494 | E1-2 | 9.7 | 15.8 | | 16.8 |
| NGC 4548 (M91) | SBB(rs) | 16.8 | 17.9 | | 15.0 |
| NGC 4552 (M89) | E | 16.8 | 14.3 | | 19.6 |
| NGC 4579 (M58) | SAB(rs)b | 16.8 | | | 21.0 |
| NGC 4594 (M104) | SA(s)a | 9.2 | 9.1 | 9.6 | 9.3 |
| NGC 4636 | E/S0 | 17.0 | 13.6 | 18.1 | |
| NGC 4736 (M94) | (R)SA(r)ab | 4.3 | 4.8 | 4.4 | 4.7 |
| NGC 5055 (M63) | SA(rs)bc | 7.2 | | | |
| NGC 5866 | S0 | 15.3 | 14.3 | 15.1 | |
| NGC 6500 | SAab | 39.7 | | | |
| NGC 7331 | SA(s)b | 14.3 | 12.2 | | 14.5 |

^a Host galaxy Hubble types were taken from the catalog of Tully (1988).

^b Distances from the catalog of Tully (1988).

^c Distances obtained using the surface brightness fluctuation method. See Tonry et al. (2001). Following Jensen et al. (2003), we have corrected the distance modulus reported by Tonry et al. (2001) by subtracting 0.16 mag.

^d Distances obtained using the planetary nebula luminosity function method. See Herrmann et al. (2008) for NGC 4736 and compilation of Ciardullo et al. (2002) and references therein for other galaxies.

^e Distances obtained using a variety of different methods, as follows: NGC 404, NGC 3031, and NGC 4736 using the tip of the red giant branch (TRGB) method Karachetsev et al. (2002) (the distance to NGC 3031 obtained by the Cepheid method by Freedman et al. 1994, agrees exactly with the TRGB distance); NGC 4261, NGC 4552, and NGC 4636 using the fundamental plane relation (see Gavazzi et al. 1999); NGC 4438, NGC 4457, and NGC 4579 using Tully-Fisher method (see Gavazzi et al. 1999); NGC 3031, NGC 4548 and NGC 7331 using the Cepheid variable method (Freedman et al. 2001, 1994).

types, the LINER types according to Ho et al. (1997b) of our sample galaxies, and the black hole masses derived from the stellar velocity dispersion. We describe and discuss the data below.

2.1. Distances

We have compiled distance measurements from the literature that are based on a variety of techniques, which we include in Table 1. All 35 galaxies have distances cataloged in Tully (1988), which were determined using a model for peculiar velocities and assuming $H_0 = 75 \text{ km s}^{-1} \text{ Mpc}^{-1}$. These are listed in column (3) of Table 1. For a significant fraction of the galaxies in our collection, distance measurements based

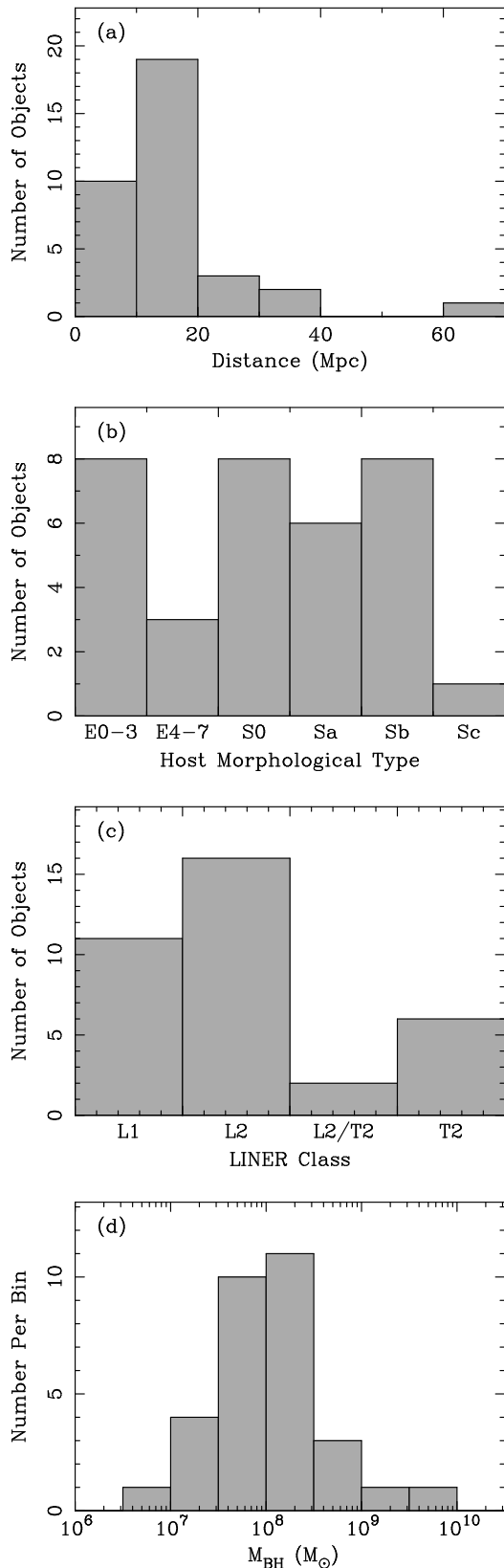


FIG. 1.— Distribution of the basic properties of the host galaxies of the sample LINERs. The black hole masses in panel (d) were derived from the stellar velocity dispersions, using equation (1). NGC 266, NGC 3507, and NGC 4438 are not included in the last histogram because their black hole masses are not available. NGC 404 is also not plotted in the last histogram because it is out of range, with $\log(M/M_{\odot}) = 5.3$.

on more direct techniques are available, which we also list in Table 1. More specifically, 24 galaxies have had their distances determined via surface brightness fluctuations (SBF) by Tonry et al. (2001), which we list in column (4) of Table 1 after making a systematic correction of -0.16 mag to the distance modulus, following Jensen et al. (2003). In column (5) of Table 1, we list distances to 8 galaxies, determined via the planetary nebula luminosity function (PNLF) method and drawn mostly from the compilation of Ciardullo et al. (2002), and references therein. Distances determined by any other method are included in column (6) of Table 1. In this paper, we adopt the distances from Tully (1988) so that the luminosities we derive can be compared directly to other quantities reported by Ho et al. (1997b), who used the same distances (e.g. emission line luminosities). None of the conclusions of this paper or paper II depend sensitively on the distance. However, we emphasize that different applications (e.g., detailed study and modeling of the SEDs) may require a more accurate distance than that of Tully (1988). In such a case the data and derived quantities we present here can be easily converted to a different distance, via a simple scaling.

2.2. Spectroscopic Classification and LINER Types

In column (5) of Table 2 we list the LINER types according to Ho et al. (1997b), which are based on the relative intensities of the narrow emission lines. The objects included in our sample are classified in this scheme either as pure LINERs (denoted by L), or as transition objects, with diagnostic line ratios intermediate between LINERs and H II regions. In about 1/3 of the objects in this sample, there are detectable broad wings on the $H\alpha$ line Ho et al. (1997c); these are termed “type 1.9” LINERs and are identified with a “1” in column (5) of Table 2, while all other objects are labeled with a “2.” If there was any ambiguity or uncertainty in the classification, both possible classes are listed. The nucleus of M81 has an uncertain classification; it can be either a LINER or a Seyfert. Since the work of Ho et al. (1997b), more recent classification schemes using the same diagnostic line ratios have become available, such as those of Kewley et al. (2001), Kauffmann et al. (2003), and Kewley et al. (2006). Thus, we have applied these classification schemes to the relative intensities of diagnostic lines measured by Ho et al. (1997b) and report the outcome of this exercise in column (6) of Table 2. We list the location of each nucleus in the $[O\text{ I}]/H\alpha$ vs $[O\text{ III}]/H\beta$, $[N\text{ II}]/H\alpha$ vs $[O\text{ III}]/H\beta$, and $[S\text{ II}]/H\alpha$ vs $[O\text{ III}]/H\beta$ diagrams, with L denoting the LINER region, S denoting the Seyfert region, H denoting the H II region, and C denoting the “composite” region in the $[N\text{ II}]/H\alpha$ vs $[O\text{ III}]/H\beta$ diagram (intermediate between LINERs or Seyferts and H II regions). Using these criteria, six objects are classified as “S/L/S,” however they fall very close to the Seyfert-LINER boundary in the $[O\text{ I}]/H\alpha$ vs $[O\text{ III}]/H\beta$ and $[S\text{ II}]/H\alpha$ vs $[O\text{ III}]/H\beta$ diagrams. Similarly, NGC 4314 is classified as “L/C/H” but it falls very close to the Composite-LINER and H II-LINER boundaries in $[N\text{ II}]/H\alpha$ vs $[O\text{ III}]/H\beta$, and $[S\text{ II}]/H\alpha$ vs $[O\text{ III}]/H\beta$ diagrams, respectively.

The mix of LINER types in our sample is dictated by the availability of data. Therefore, there may be some biases inherited from the surveys from which we adopted the data. More specifically, the surveys we have relied on targeted radio-bright, UV-bright, and X-ray bright objects. Thus, we find that “transition” objects (according to Ho et al. 1997b) are under-represented in our sample relative to their number in the survey of Ho et al. (1997a), while “type 1.9” LINERs are over-represented. We also note that our search for data, al-

TABLE 2
PROPERTIES OF LINER NUCLEI

| Galaxy (1) | Galactic | | log (M_{BH}/M_{\odot}) ^c | LINER Type | |
|---------------|------------------------------------|---|---|------------------------|----------------------------|
| | $E(B-V)$ ^a (mag) (2) | σ_* ^b (km s^{-1}) (3) | | Ho ^d (5) | Kewley ^e (6) |
| NGC 0266 | 0.069 | ... | ... | L1 | L/L/L |
| NGC 0404 | 0.059 | 40 | 5.3 | L2 | L/C/L |
| NGC 1097 | 0.027 | 196 | 8.1 | L1 | L/L/S |
| NGC 1553 | 0.013 | 177 | 7.9 | L2/T2 | ?L/? |
| NGC 2681 | 0.023 | 108 | 7.1 | L1 | L/L/H |
| NGC 3031 | 0.080 | 162 | 7.8 | S1.5/L1 | L/L/S |
| NGC 3169 | 0.031 | 163 | 7.8 | L2 | L/L/L |
| NGC 3226 | 0.023 | 193 | 8.1 | L1 | L/L/L |
| NGC 3379 | 0.024 | 207 | 8.2 | L2/T2 | L/L/L |
| NGC 3507 | 0.024 | ... | ... | L2 | L/L/H |
| NGC 3607 | 0.021 | 224 | 8.4 | L2 | L/L/S |
| NGC 3608 | 0.021 | 192 | 8.1 | L2/S2 | S/L/S |
| NGC 3628 | 0.027 | 171 | 7.9 | T2 | S/L/S |
| NGC 3998 | 0.016 | 305 | 8.4 | L1 | L/L/S |
| NGC 4111 | 0.015 | 148 | 7.6 | L2 | L/L/H |
| NGC 4125 | 0.019 | 227 | 8.4 | T2 | L/L/L |
| NGC 4143 | 0.013 | 214 | 8.3 | L1 | L/L/L |
| NGC 4261 | 0.018 | 309 | 8.7 | L2 | L/L/L |
| NGC 4278 | 0.029 | 261 | 8.6 | L1 | L/L/L |
| NGC 4314 | 0.025 | 117 | 7.2 | L2 | L/C/H |
| NGC 4374 | 0.040 | 308 | 9.2 | L2 | L/L/L |
| NGC 4438 | 0.028 | ... | ... | L1 | L/L/L |
| NGC 4457 | 0.022 | 96 | 6.9 | L2 | L/L/H |
| NGC 4486 | 0.022 | 333 | 9.5 | L2 | L/L/L |
| NGC 4494 | 0.021 | 145 | 7.6 | L2 | L/L/L |
| NGC 4548 | 0.038 | 144 | 7.6 | L2 | L/L/L |
| NGC 4552 | 0.041 | 203 | 8.2 | T2 | L/L/L |
| NGC 4579 | 0.041 | 165 | 7.8 | L1 | L/L/L |
| NGC 4594 | 0.051 | 241 | 9.0 | L2 | L/L/L |
| NGC 4636 | 0.028 | 203 | 8.2 | L1 | L/L/L |
| NGC 4736 | 0.018 | 112 | 7.1 | L2 | L/L/L |
| NGC 5055 | 0.018 | 108 | 7.1 | T2 | L/L/H |
| NGC 5866 | 0.013 | 159 | 7.7 | T2 | S/L/S |
| NGC 6500 | 0.090 | 214 | 8.3 | L2 | L/C/L |
| NGC 7331 | 0.091 | 138 | 7.5 | T2 | S/L/S |

^a Reddening caused by the ISM of the Milky Way; from Schlegel et al. (1998).

^b The stellar velocity dispersion, taken from the Hypercat database, with the following exceptions: NGC 404, NGC 4278, NGC 4314, NGC 4374, NGC 4579, NGC 4736, NGC 5055, NGC 6500 from Barth et al. (2002); NGC 1097 from Lewis & Eracleous (2006).

^c The log of the black hole mass in M_{\odot} . Derived from stellar velocity dispersions using equation (1), with the following exceptions: for NGC 3031 it was derived from stellar and gas kinematics (Bower et al. 2000; Devereux et al. 2003), while for NGC 4261 and NGC 4374 it was derived from gas kinematics (Ferrarese et al. 1996; Bower et al. 1998).

^d Spectroscopic classification according to Ho et al. (1997b), with the exception of NGC 1097 and NGC 1553. The LINER types for these two galaxies were taken from Phillips et al. (1984) and Phillips et al. (1986), respectively. L1=LINER with a broad H α line, L2=LINER without a broad H α line, T2=intermediate emission line ratios between LINER and H II region, S=Seyfert; combinations indicate intermediate line ratios between two classes.

^e Spectroscopic classification based on the criteria of Kewley et al. (2001), Kauffmann et al. (2003), and Kewley et al. (2006). The three designations refer to the location of the object in the [O I]/H α vs [O III]/H α , [N II]/H α vs [O III]/H α , and [S II]/H α vs [O III]/H α diagrams, respectively. L=LINER, S=Seyfert, H=H II region, C=“composite,” i.e., intermediate between LINERs or Seyferts and H II regions in the [N II]/H α vs [O III]/H α diagram.

though extensive, was not exhaustive, with the result that we may have overlooked a few objects. It is not clear whether the relative number of LINER types in our sample should have an effect on our conclusions. If the properties of the AGN are related to the LINER class, then the composition of the sample may influence any average properties derived from it. We attempt to assess such effects at the end of §4.1 using our estimated bolometric luminosities.

2.3. Stellar Velocity Dispersions and Black Hole Masses

The stellar velocity dispersions of the sample galaxies were taken from the Hypercat database⁶, with the following exceptions: the values for NGC 404, NGC 4278, NGC 4314, NGC 4579, NGC 4736, NGC 5055, NGC 6500 are from Barth et al. (2002), while the value for NGC 1097 is from Lewis & Eracleous (2006). The black hole masses were estimated from the stellar velocity dispersions via the $M_{\text{BH}}-\sigma_*$ relationship (Ferrarese & Merritt 2000; Gebhardt et al. 2000; Tremaine et al. 2002), namely,

$$\log(M/M_{\odot}) = \alpha + \beta \log(\sigma_*/\sigma_0), \quad (1)$$

where $\alpha = 8.13 \pm 0.06$, $\beta = 4.02 \pm 0.32$, and $\sigma_0 = 200 \text{ km s}^{-1}$ (Tremaine et al. 2002). For the following galaxies we adopt the black hole masses measured from spatially resolved stellar and/or gas kinematics: NGC 3031 (Bower et al. 2000; Devereux et al. 2003), NGC 3998 (de Francesco et al. 2006) NGC 4261 (Ferrarese et al. 1996), NGC 4374 (Bower et al. 1998), NGC 4486 (Machetto 1997), and NGC 4594 (Kormendy et al. 1996). In the case of NGC 3031 separate measurements from stellar kinematics, gas kinematics, and the central stellar velocity dispersion give nearly identical values (within 5%). In the case of NGC 4261, the black hole mass from gas kinematics differs from that obtained from the central stellar velocity dispersion by a factor of only 1.6. In seven cases where the stellar velocity dispersion is reported both in the Hypercat database and by Barth et al. (2002), the black hole masses are within a factor 1.6 or less from each other. There are four large discrepancies, as follows: in NGC 404 where the stellar velocity dispersions reported in the Hypercat database and by Barth et al. (2002) lead to black hole masses that differ by a factor of 3.6, while in NGC 3998, NGC 4486, and NGC 4594 mass determinations from the central stellar velocity dispersion and spatially resolved stellar or gas kinematics differ by factors between 2.7 and 3.5. Considering all cases with multiple determinations of the black hole mass, the values of $\Delta \log(M/M_{\odot})$ are evenly distributed about zero with a standard deviation of 0.34 (amounting to a factor of approximately 2). There are three galaxies for which we could not estimate the black hole masses because we could not find the necessary data: NGC 266, NGC 3507, and NGC 4438. The distribution of black hole masses is shown in Figure 1d. Their values span the range $5.3 < \log(M/M_{\odot}) < 9.5$.

3. SPECTRAL ENERGY DISTRIBUTIONS

3.1. Data Compilation

In Table 3 we present the data making up the SEDs of individual galaxies in the form of monochromatic luminosity versus frequency (i.e., νL_{ν} vs ν). These data were taken from sources in the literature, as listed in Table 3. We include in this table monochromatic luminosities with and without corrections for extinction (see discussion of extinction corrections below). As we noted in §2, we include primarily measurements made at high spatial resolution ($< 1''$); in some cases observations at lower spatial resolution are used, but the resulting measurements are treated as upper limits. Upper limits from non-detections are also listed in this table. In cases where UV (2500 Å) measurements or limits are not available but X-ray measurements or upper limits are, we inferred

⁶ <http://www-obs.univ-lyon1.fr/hypercat>

UV upper limits from the 2 keV monochromatic luminosities and the assumption that the optical-to-X-ray spectral index is $\alpha_{\text{ox}} < 1.5$. We justify this assumption in §4.1, below. Column (3), labeled “Observed νL_ν ,” gives the monochromatic luminosity obtained from the observed flux density without any corrections. Columns (4) and (5), labeled “Corrected νL_ν ,” give the monochromatic luminosity after minimum (following Calzetti et al. 1994) and maximum (following Seaton 1979) extinction corrections. We discuss these corrections in detail in §3.2 below. The individual SEDs are shown graphically in Figure 2, in a separate panel for each galaxy; the “Observed νL_ν ” is represented by filled points, with arrows denoting upper limits, while open points show νL_ν after the maximum extinction correction.

With the exception of the X-ray data, measurements were made in relatively narrow bands ($\Delta\nu/\nu \lesssim 0.2$), centered at a specific frequency. Whenever multiple measurements were available at approximately the same frequency, these were averaged together and their fractional standard deviations, $\sigma/(\nu L_\nu)$, are given in a separate column of Table 3. These variations can be caused by intrinsic variability of the source (specifically in the near UV; cf, Maoz et al. 2005) or differences in spatial resolution. In the former case the temporal fluctuations are often less than 10% on time scales of about a year. However, Maoz et al. (2005) have also found some examples of larger variations (up to 50%) on these short time scales. More importantly, they have found that on time scales of several years to a decade the amplitude of the fluctuations can reach a factor of a few. In the case of near-IR and radio data, the fluctuations can be as large as $\sim 60\%$. We have also encountered an example of even more extreme variability in the radio band, which we discuss briefly in §3.3.

The X-ray data are in the form of broad-band spectra, typically spanning the energy range 0.5–10 keV. Many of the X-ray spectra can be fitted with simple power-law models, modified by interstellar photoelectric absorption in nearly neutral gas. In some cases, more complex models are needed, consisting of a power law plus optically thin emission from a thermal plasma (see, for example, Eracleous et al. 2002; Flohic et al. et al. 2006, and references therein). In such cases, the power-law component is attributed to the AGN and the thermal plasma component is ascribed to spatially-unresolved, circumnuclear emission. Thus, we have taken the power-law component from such models to represent the emission from the AGN. In all cases, we adopt the power-law model as a convenient parameterization of the data. This model describes the intrinsic photon energy spectrum (number of emitted photons per unit energy interval) as $N(E) = N_0(E/E_0)^{-\Gamma}$, where E_0 is a fiducial energy (typically $E_0 = 1$ keV), Γ is known as the “photon index,” and $N_0 = N(E_0)$ is the “normalization constant” (with units of $\text{cm}^{-2} \text{s}^{-1} \text{keV}^{-1}$). With this convention, and keeping in mind that $f_\nu(E_0) = h N_0 E_0$ (where h is Planck’s constant), we can write the flux density spectrum as

$$f_\nu(E) = f_\nu(E_0) \left(\frac{E}{E_0} \right)^{1-\Gamma} \\ = 0.663 \left(\frac{N_0}{1 \text{ cm}^{-2} \text{ s}^{-1} \text{ keV}^{-1}} \right) \left(\frac{E}{1 \text{ keV}} \right)^{1-\Gamma} \text{ mJy}. \quad (2)$$

The parameters describing the power-law X-ray spectrum (Γ and N_0 , for $E_0 = 1$ keV), as well as the equivalent hydrogen column density (N_{H} ; inferred from fitting the model to the

data) are listed in Table 4. Using these parameters we have calculated the values of νL_ν at 0.5, 1, and 10 keV, which we list in Table 3 (the three highest-frequency values for each object). We note that the AGNs in LINERs are typically detected at 0.5 and 1 keV, and often also at 10 keV, so it is fair to use the models to evaluate νL_ν at these energies. In Figure 2 we plot the X-ray component of the SED as a thick solid line between 0.5 and 10 keV (already corrected for extinction) and we extrapolate it to 100 keV, although only for reference.

In a number of cases, the X-ray emission from the AGN is not detected, but an upper limit is available from the observations. These limits are expressed in Table 4 as upper limits on the normalization of the X-ray spectrum, for an assumed value of a photon index of $\Gamma = 1.8$.⁷ In the case of one galaxy, NGC 3379, the normalization of the X-ray spectrum is not an upper limit but it was derived under the assumption of $\Gamma = 1.8$, because of the low S/N of the X-ray spectrum. The monochromatic luminosities of these objects given in Table 3 are also identified as upper limits.

3.2. Extinction Corrections

To facilitate extinction corrections, we have listed the values of the color excess (or reddening), $E(B - V)$, associated with the Galactic ISM (taken from Schlegel, Finkbeiner, & Davis, 1998) in Table 2. The model fits to the X-ray spectra yield a value for the *total* equivalent hydrogen column density (N_{H} , listed in Table 4). These models typically assume the photoelectric absorption cross-sections of Morrison & McCammon (1983), who adopted the elemental abundances of Anders & Ebihara (1982). In Table 4, we also list the corresponding value of the *total* color excess, derived from the following relation between the visual extinction, A_V , and the hydrogen column density (from Predehl & Schmitt 1995, applicable to the Milky Way)

$$N_{\text{H}}/A_V = 1.79 \times 10^{21} \text{ cm}^{-2} \text{ mag}^{-1}, \quad (3)$$

and assuming that $R_V \equiv A_V/E(B - V) = 3.2$. As expected, in most cases the *total* reddening, $E(B - V)_X$ corresponding to the hydrogen column determined from the X-ray spectra, is larger than the reddening caused by the Galactic ISM. In two cases, NGC 404 and NGC 3031, $E(B - V)$ exceeds $E(B - V)_X$ by 0.019 and 0.008 magnitudes respectively, which is well within the uncertainties of the column densities derived from X-ray observations. In Figure 3a, we show the distribution of values of $E(B - V)_X$ of the objects in our sample to illustrate that $E(B - V)_X < 0.6$ in about 31/33 of the objects and $E(B - V)_X < 0.2$ in about 22/33 of the objects (we exclude 2 objects with extremely high extinction, in which no meaningful correction can be made). The values of $E(B - V)_X$ should be regarded with caution because of the assumptions involved in deriving them. Most uncertain is the assumption of a Galactic gas-to-dust ratio, which is inherent in the relation between the hydrogen column density and the visual extinction given in equation (3). Furthermore, there is also the possibility that the lines of sight to the UV and X-ray sources do not pass through exactly the same column of absorbing material.

We applied extinction corrections to the observed monochromatic luminosities as follows: Using the values of the *total* reddening, $E(B - V)_X$, for each galaxy

⁷ This value of Γ is the median value found in the large sample of Flohic et al. et al. (2006). The derived limits are not very sensitive to the value of Γ (see the discussion in Flohic et al. et al. 2006, and footnote (a) in Table 4). For example, changing Γ by ± 0.2 changes the flux by only $\sim 10\%$.

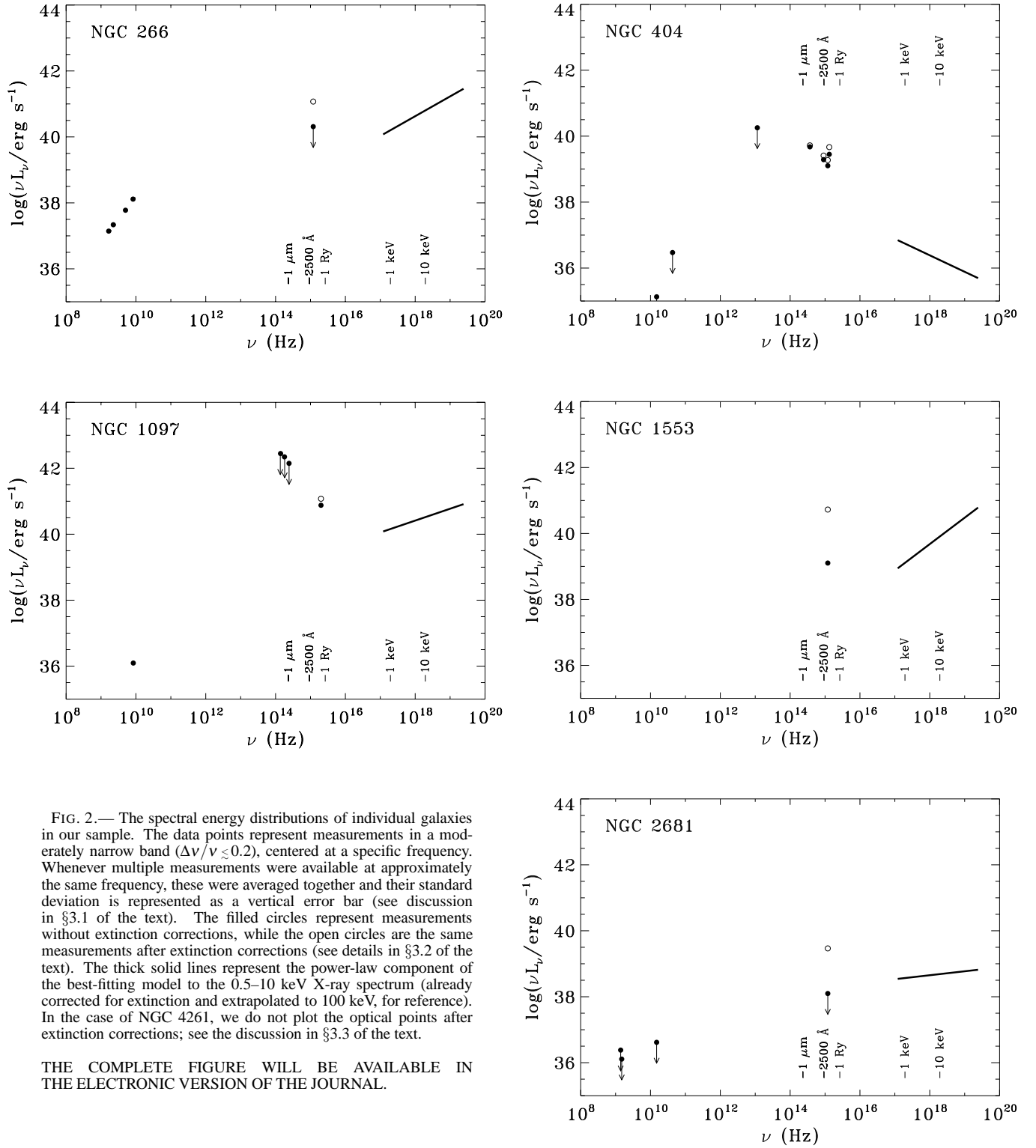


FIG. 2.— The spectral energy distributions of individual galaxies in our sample. The data points represent measurements in a moderately narrow band ($\Delta\nu/\nu \lesssim 0.2$), centered at a specific frequency. Whenever multiple measurements were available at approximately the same frequency, these were averaged together and their standard deviation is represented as a vertical error bar (see discussion in §3.1 of the text). The filled circles represent measurements without extinction corrections, while the open circles are the same measurements after extinction corrections (see details in §3.2 of the text). The thick solid lines represent the power-law component of the best-fitting model to the 0.5–10 keV X-ray spectrum (already corrected for extinction and extrapolated to 100 keV, for reference). In the case of NGC 4261, we do not plot the optical points after extinction corrections; see the discussion in §3.3 of the text.

THE COMPLETE FIGURE WILL BE AVAILABLE IN THE ELECTRONIC VERSION OF THE JOURNAL.

TABLE 3
SPECTRAL ENERGY DISTRIBUTIONS OF INDIVIDUAL LINERs

| Galaxy (1) | ν (Hz) (2) | Observed νL_ν (erg s ⁻¹) (3) | Corrected νL_ν (erg s ⁻¹) ^a | | $\sigma / \langle \nu L_\nu \rangle^b$ (6) | References ^c and Notes (7) | |
|---------------|------------------------|--|---|-------------------------|---|---|---|
| | | | Calzetti (min) (4) | Seaton (max) (5) | | | |
| NGC 266 | 1.700×10^9 | 1.43×10^{37} | ... | ... | | 1 | d |
| | 2.300×10^9 | 2.14×10^{37} | ... | ... | | 1 | d |
| | 5.000×10^9 | 6.06×10^{37} | ... | ... | | 1 | d |
| | 8.400×10^9 | 1.41×10^{38} | ... | ... | | 1 | d |
| | 1.199×10^{15} | $< 2.05 \times 10^{40}$ | $< 1.18 \times 10^{41}$ | $< 2.88 \times 10^{41}$ | | | e |
| | 1.210×10^{17} | 1.20×10^{40} | ... | ... | | 2 | |
| | 2.420×10^{17} | 1.81×10^{40} | ... | ... | | 2 | |
| | 2.420×10^{18} | 7.22×10^{40} | ... | ... | | 2 | |
| NGC 404 | 1.500×10^{10} | $< 1.34 \times 10^{35}$ | ... | ... | | 3 | f |
| | 4.286×10^{10} | $< 2.95 \times 10^{36}$ | ... | ... | | 4 | f |
| | 1.149×10^{13} | $< 1.80 \times 10^{40}$ | ... | ... | | 5 | g |
| | 3.686×10^{14} | 4.74×10^{39} | 4.74×10^{39} | 5.26×10^{39} | | 6 | |
| | 9.085×10^{14} | 1.94×10^{39} | 2.06×10^{39} | 2.58×10^{39} | | 7 | h |
| | 1.199×10^{15} | 1.27×10^{39} | 1.39×10^{39} | 1.88×10^{39} | | 7 | h |
| | 1.322×10^{15} | 2.82×10^{39} | 3.12×10^{39} | 4.65×10^{39} | | 8 | |
| | 1.210×10^{17} | 7.00×10^{36} | ... | ... | | 9 | |
| | 2.420×10^{17} | 4.95×10^{36} | ... | ... | | 9 | |
| | 2.420×10^{18} | 1.57×10^{36} | ... | ... | | 9 | |

THE COMPLETE TABLE WILL BE AVAILABLE IN THE ELECTRONIC VERSION OF THE JOURNAL

^a The monochromatic luminosities from 0.1 to $1\mu\text{m}$ after correction for extinction. The minimum correction employs the starburst extinction law of Calzetti et al. (1994), while the maximum correction corresponds to the Milky Way law of Seaton (1979). Details are given in §S:data of the text. The “observed” X-ray luminosities already have this correction built in. The distances used are those of Tully (1988); see Table 1 and the discussion in §2.1 of the text.

^b The fractional dispersion in the monochromatic luminosity in cases where a number of measurements were averaged together. See §3.1 of the text for details.

^c *References.* – (1) Doi et al. (2005a); (2) Terashima & Wilson (2003); (3) Nagar et al. (2005); (4) Nagar et al. (2000); (5) Saryapal et al. (2004); (6) Chiaberge et al. (2005); (7) Maoz et al. (2005); (8) Maoz et al. (1995); (9) Eracleous et al. (2002).

^d See detailed notes on this object in §3.3 of the text.

^e Upper limit to $\nu L_\nu(2500 \text{ \AA})$ derived by assuming $\alpha_{\text{ox}} = 1.5$. See §4.1 of the text for details.

^f This limit is a result of a non-detection.

^g This limit is a result of contamination of the source by other, neighboring sources; the observations were taken through a large aperture.

^h The observed UV flux most likely originates in hot stars in the immediate vicinity of the nucleus, not in the AGN. See the discussion in §3.3 of the text. The values of α_{ox} implied by the UV flux is extremely high for such a low-luminosity AGN thus, the UV flux listed here can be taken as a *generous* upper limit to the UV flux of the AGN.

we computed the extinction corrections for points in the SED between 0.1 and 1 μm using the following five extinction laws: the Milky Way extinction laws of Seaton (1979) and Cardelli, Clayton, & Mathis (1989), the Large and Small Magellanic Cloud extinction laws of Korneef & Code (1981) and Bouchet et al. (1985), respectively, and the starburst galaxy extinction law of Calzetti, Kinney, & Storchi-Bergmann (1994).

All of the Milky Way and Magellanic Cloud laws agree well with each other in the near-IR, optical, and near-UV bands but not in the far UV (see, for example, Figures 1 and 21 in Calzetti et al. 1994). The differences are most pronounced in the far-UV band, at $\lambda < 1500 \text{ \AA}$. In the near-UV the Milky Way and LMC extinction curves are not monotonic (because of the “2200 \AA bump”) with the result that the curves cross each other. Thus, the law that gives the highest extinction correction changes with wavelength and also with the value of $E(B-V)_X$. To illustrate the effects of and differences between the above extinction laws, we plot in Figures 3b and 3c, respectively, the transmission factor (i.e., the fraction of flux that is transmitted) at 2500 \AA according to each of the extinction laws and the relations between the different transmission factors. The starburst extinction law of Calzetti et al. (1994) differs considerably from the other four laws. Considering the Milky Way and Magellanic Cloud extinction laws, we find that for $E(B-V)_X < 0.2$ (22/33 of our objects) the transmission factors range between 0.29 and 0.32 and for $E(B-V)_X < 0.5$ (31/33 of our objects) the transmission factors range between 0.02 and 0.03.

In the end we adopted the Seaton (1979) law, which leads to the largest corrections. We note, however, that if we had adopted any other of the Milky Way or Magellanic Cloud laws, the difference in the corrected flux would have been of order 10% or less. The resulting, corrected monochromatic luminosities are also included in column (5) of Table 3. For reference, in column (4) of Table 3 we also list the monochromatic luminosity after correcting with the starburst extinction law of Calzetti, Kinney, & Storchi-Bergmann (1994), which yields the minimum correction compared to the other laws.

We draw attention to the uncertainties involved in our extinction corrections: the most important uncertainty is the assumption of the Milky Way dust-to-gas ratio, which is incorporated into equation (3), and our adopted value of $R_V = 3.2$. We also emphasize that the extinction corrections we adopted are suitable for our specific application (assessing the energy budgets of LINERs; see paper II), but may not be appropriate for other applications. More specifically, in paper II we estimate the ionizing luminosities of the weak AGNs in this sample in order to assess whether they can power the observed emission lines. Therefore, we take the highest possible extinction correction so as to err on the side of caution, i.e., to overestimate the UV luminosity rather than underestimate it.

3.3. Notes on Individual Objects

NGC 266. – The radio properties of the AGN in NGC 266 have been studied by Doi, Kameno, & Inoue (2005a) using observations at multiple epochs. They found significant variability in both the radio luminosity and the shape of the radio spectrum. Here we adopt their data from VLBA observations taken on a single epoch, 2003 March 8.

NGC 404. – A UV spectrum of the nucleus of this galaxy shows prominent absorption features from hot stars

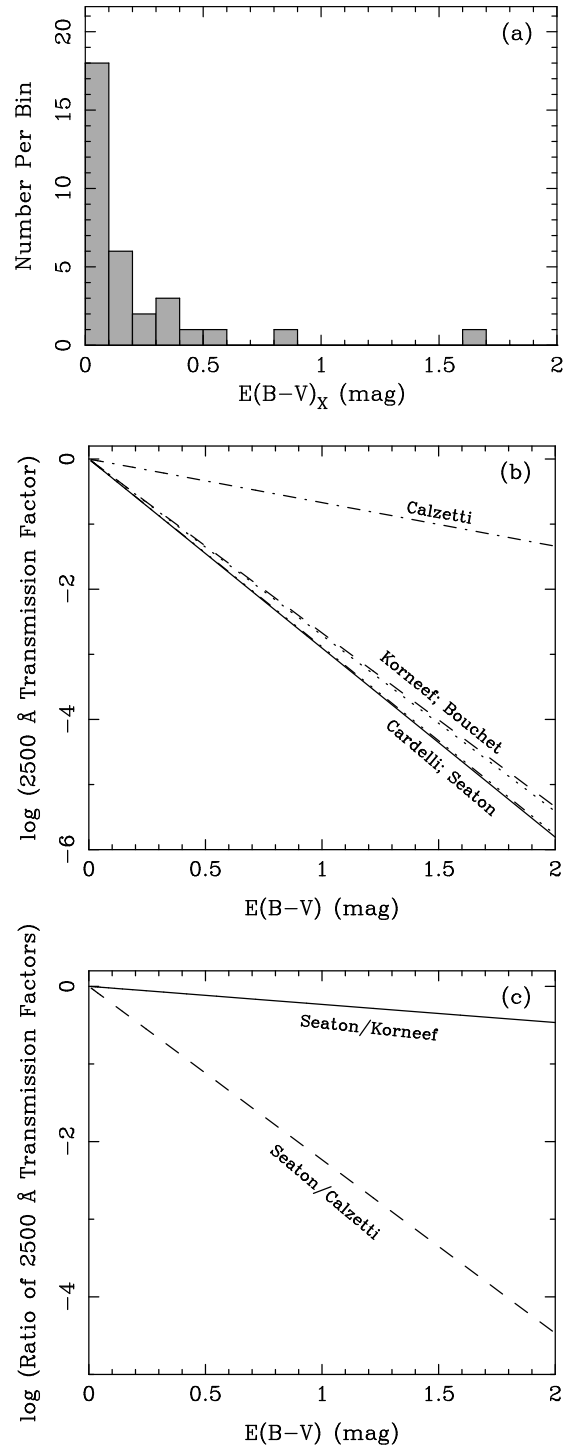


FIG. 3.— Reddening values and extinction corrections for 33 of the 35 objects in our sample (NGC 3169 and NGC 4261 are excluded because the column density is so large that they should be invisible in the UV). (a) The distribution of the values of $E(B-V)_X$, the reddening derived from the X-ray column density (listed in Table 4). As this histogram shows, 31/33 objects have $E(B-V)_X < 0.6$ and 22/33 objects have $E(B-V)_X < 0.2$. (b) The fraction of transmitted flux at 2500 \AA for the five extinction laws that we have explored, with line styles as follows (top to bottom): dot-dashed for the Starburst law of Calzetti et al. (1994), dashed for the LMC law of Korneef & Code (1981), dotted for the LMC law of Bouchet et al. (1985), and triple-dot-dashed and solid for the Milky Way laws of Cardelli et al. (1989) and Seaton (1979), respectively. (c) Comparison of extinction laws via the ratios of 2500 \AA transmission factors. The “Seaton/Calzetti” ratio represents the full range of possible extinction corrections, while the “Seaton/Korneef” ratio represents the range of possible non-starburst corrections.

TABLE 4
X-RAY SPECTRAL PARAMETERS AND DERIVED PROPERTIES

| X-Ray Spectral Parameters | | | | | | | | |
|---------------------------|-------------------|--|---|------------------------------|--|--|-----------------------------------|-------------------------------|
| Galaxy (NGC) (1) | Γ^a (2) | N_0 ($\text{cm}^{-2} \text{s}^{-1}$) (3) | N_{H} (cm^{-2}) (4) | $E(B-V)_X^b$ (mag) (5) | $L_{2-10\text{keV}}$ (erg s^{-1}) (6) | L_{bol}^c (erg s^{-1}) (7) | \mathcal{R}_{Edd} (8) | α_{ox}^d (9) |
| 0266 | 1.40 | 5.223×10^{-6} | 1.5×10^{21} | 0.262 | 7.4×10^{40} | 2.2×10^{42} | ... | ... |
| 0404 | 2.50 | 4.490×10^{-6} | 2.3×10^{20} | 0.040 | 3.9×10^{36} | 1.2×10^{38} | 4×10^{-6} | ... |
| 1097 | 1.64 | 3.864×10^{-4} | 2.3×10^{20} | 0.040 | 4.3×10^{40} | 8.5×10^{41} | 5×10^{-5} | 1.14 |
| 1553 | 1.20 | 4.438×10^{-5} | 3.2×10^{21} | 0.559 | 8.7×10^{39} | 4.4×10^{41} | 4×10^{-5} | ... |
| 2681 | 2.00 | 4.990×10^{-6} | 2.7×10^{21} | 0.471 | 1.8×10^{38} | 9.0×10^{39} | 6×10^{-6} | ... |
| 3031 | 1.88 | 1.775×10^{-3} | 4.1×10^{20} | 0.072 | 1.9×10^{40} | 2.1×10^{41} | 3×10^{-5} | 1.04 |
| 3169 | 2.60 | 5.138×10^{-3} | 1.12×10^{23} | 19.55 | 1.1×10^{41} | 3.3×10^{42} | 4×10^{-4} | ... |
| 3226 | 2.21 | 4.440×10^{-4} | 9.3×10^{21} | 1.624 | 5.0×10^{40} | 1.5×10^{42} | 1×10^{-4} | ... |
| 3379 | 1.80 ^e | 6.200×10^{-7} | 2.75×10^{20} | 0.048 | 1.7×10^{37} | 5.1×10^{38} | 3×10^{-8} | ... |
| 3507 | 1.80 ^f | $< 2.400 \times 10^{-7}$ | 1.63×10^{20} | 0.029 | $< 3.9 \times 10^{37}$ | $< 1.2 \times 10^{39}$ | ... | ... |
| 3607 | 1.80 ^f | $< 3.000 \times 10^{-7}$ | 1.48×10^{20} | 0.026 | $< 5.0 \times 10^{37}$ | $< 1.5 \times 10^{39}$ | $< 5 \times 10^{-8}$ | > 0.55 |
| 3608 | 1.80 ^f | $< 2.600 \times 10^{-6}$ | 1.49×10^{20} | 0.026 | $< 5.9 \times 10^{38}$ | $< 1.8 \times 10^{40}$ | $< 1 \times 10^{-6}$ | ... |
| 3628 | 1.80 ^f | $< 2.000 \times 10^{-7}$ | 2.23×10^{20} | 0.039 | $< 4.9 \times 10^{36}$ | $< 1.5 \times 10^{38}$ | $< 2 \times 10^{-8}$ | ... |
| 3998 | 1.88 | 3.611×10^{-3} | 5.82×10^{20} | 0.102 | 2.6×10^{41} | 1.4×10^{43} | 4×10^{-4} | 1.05 |
| 4111 | 1.80 ^f | $< 3.010 \times 10^{-5}$ | 1.40×10^{20} | 0.024 | $< 3.6 \times 10^{39}$ | $< 1.1 \times 10^{41}$ | $< 2 \times 10^{-5}$ | > 1.00 |
| 4125 | 1.80 ^f | $< 2.200 \times 10^{-6}$ | 1.84×10^{20} | 0.032 | $< 5.4 \times 10^{38}$ | $< 1.6 \times 10^{40}$ | $< 6 \times 10^{-7}$ | ... |
| 4143 | 1.66 | 7.331×10^{-5} | 1.5×10^{20} | 0.026 | 1.1×10^{40} | 3.2×10^{41} | 1×10^{-5} | ... |
| 4261 | 1.56 | 1.900×10^{-4} | 5.0×10^{22} | 8.73 | 1.0×10^{41} | 6.8×10^{41} | 1×10^{-5} | ... |
| 4278 | 1.64 | 1.800×10^{-4} | 3.5×10^{20} | 0.061 | 9.1×10^{39} | 2.7×10^{41} | 5×10^{-6} | ... |
| 4314 | 2.10 | $< 1.130 \times 10^{-4}$ | 1.78×10^{20} | 0.031 | $< 3.1 \times 10^{37}$ | $< 9.2 \times 10^{38}$ | $< 5 \times 10^{-7}$ | ... |
| 4374 | 2.10 | 3.762×10^{-5} | 1.9×10^{21} | 0.332 | 3.5×10^{39} | 5.0×10^{41} | 3×10^{-6} | 0.99 |
| 4438 | 1.80 ^f | $< 9.999 \times 10^{-6}$ | 1.20×10^{21} | 0.210 | $< 1.2 \times 10^{39}$ | $< 3.5 \times 10^{40}$ | ... | > 0.88 |
| 4457 | 1.70 | 6.815×10^{-6} | 9.8×10^{20} | 0.171 | 1.0×10^{39} | 3.0×10^{40} | 3×10^{-5} | ... |
| 4486 | 2.17 | 2.310×10^{-4} | 6.1×10^{20} | 0.107 | 1.6×10^{40} | 9.8×10^{41} | 2×10^{-6} | 1.33 |
| 4494 | 1.80 | 2.352×10^{-5} | 3.0×10^{20} | 0.052 | 9.2×10^{38} | 2.8×10^{40} | 6×10^{-6} | ... |
| 4548 | 1.70 | 4.432×10^{-5} | 1.6×10^{22} | 2.793 | 5.4×10^{39} | 1.6×10^{41} | 3×10^{-5} | ... |
| 4552 | 2.00 | 6.700×10^{-6} | 6.0×10^{20} | 0.105 | 2.6×10^{39} | 7.8×10^{40} | 4×10^{-6} | 1.03 |
| 4579 | 1.50 | 2.116×10^{-5} | 2.54×10^{20} | 0.044 | 1.8×10^{41} | 1.0×10^{42} | 1×10^{-4} | 0.92 |
| 4594 | 1.89 | 2.450×10^{-4} | 1.9×10^{21} | 0.332 | 7.5×10^{39} | 4.8×10^{41} | 4×10^{-6} | 1.23 |
| 4636 | 1.80 ^f | $< 5.100 \times 10^{-6}$ | 1.81×10^{20} | 0.032 | $< 6.1 \times 10^{38}$ | $< 1.8 \times 10^{40}$ | $< 1 \times 10^{-6}$ | > 1.14 |
| 4736 | 1.60 | 5.600×10^{-5} | 3.3×10^{20} | 0.058 | 5.9×10^{38} | 1.8×10^{40} | 1×10^{-5} | 1.36 |
| 5055 | 1.80 | 2.843×10^{-5} | 5.0×10^{21} | 0.873 | 2.0×10^{38} | 5.9×10^{39} | 4×10^{-6} | ... |
| 5866 | 1.80 ^f | $< 3.199 \times 10^{-6}$ | 1.47×10^{20} | 0.024 | $< 3.1 \times 10^{38}$ | $< 9.4 \times 10^{39}$ | $< 1 \times 10^{-6}$ | > 0.81 |
| 6500 | 3.10 | 5.178×10^{-5} | 2.1×10^{21} | 0.367 | 5.3×10^{39} | 1.6×10^{41} | 7×10^{-6} | ... |
| 7331 | 1.80 ^f | $< 4.001 \times 10^{-7}$ | 8.61×10^{20} | 0.150 | $< 3.4 \times 10^{37}$ | $< 1.0 \times 10^{39}$ | $< 3 \times 10^{-7}$ | > 1.33 |

^a The typical uncertainty in Γ is $\pm 0.2-0.3$. The fractional uncertainty in the X-ray flux is dominated by the uncertainty in Γ and is given by $\delta f_X / f_X = 0.69 \delta \Gamma$. Thus, fractional uncertainties in the X-ray flux are of order 10–20%.

^b The reddening corresponding to the equivalent hydrogen column density reported in this table, obtained using equation (3) in §3.1 of the text.

^c The bolometric luminosity of NGC 3031, NGC 3998, NGC 4261, NGC 4374, NGC 4486, NGC 4579, and NGC 4594 was determined by integrating the S.E.D. The bolometric luminosity of NGC 1097 was derived from a model fit to the SED (see §3.3). For all other galaxies the bolometric luminosity was obtained by scaling the 2–10 keV X-ray luminosity as discussed in §4.1 of the text.

^d The optical-to-X-ray spectral index, defined in §4.1 of the text. The tabulated values were computed after correcting the UV flux according to the Seaton (1979) law and using the values of $E(B-V)_X$ from column (5) of this table (maximal correction). Typical uncertainties on α_{ox} are ≥ 0.03 and can be as high as 0.09 (see the discussion in §4.1 of the text).

^e Because of the low S/N of the X-ray spectrum, the X-ray photon index was assumed to be $\Gamma = 1.8$ for the purpose of deriving a value for the normalization. The normalization itself and resulting X-ray flux are not upper limits, but are subject to the assumed value of Γ .

^f The X-ray photon index was assumed to be $\Gamma = 1.8$ for the purpose of deriving an upper limit to the normalization and the X-ray flux.

(Maoz et al. 1998), indicating that they make a significant contribution to the light at these wavelengths. The X-ray spectrum is very soft (see the discussion in Eracleous et al. 2002), with $\Gamma = 2.5$, which is uncharacteristic of AGNs (cf, Nandra et al. 1997), although an AGN cannot be ruled out based on this observation. The nuclear source is resolved at both UV and X-ray wavelengths and it has a “blow-out” morphology (Maoz et al. 1995; Eracleous et al. 2002). On the other hand, the compact nucleus of the UV source appears to be variable by a factor of approximately two on a time scale of approximately a decade. In addition, the depths of the absorption lines appear to be shallower than the

those found in the spectra of hot stars (Maoz et al. 2005; Maoz 2007). All of these properties suggest that the nucleus of NGC 404 harbors a compact star-forming region as well as a low-luminosity AGN. Therefore, we include this object in our sample.

NGC 1097. – The SED of the AGN in NGC 1097 and model fits to it are discussed by Nemmen et al. (2006). Here, we adopted a subset of the data included in that paper. The IR measurements presented by Prieto et al. (2005) were taken through a very small aperture, which isolates the nucleus. However, the AGN is embedded in an compact, unresolved star-

burst (Storchi-Bergmann et al. 2005) which may dominate the emission at these wavelengths, therefore, we have designated these measurements as upper limits to the flux of the AGN. We excluded measurements taken through large apertures since these were significantly contaminated by emission from the circumnuclear starburst ring. A significant fraction of the nuclear UV flux appears to originate from a compact starburst, as suggested by absorption lines from hot stars detected in the *HST* spectrum (Storchi-Bergmann et al. 2005; Nemmen et al. 2006). By following the best-fitting SED model of (Nemmen et al. 2006), we adopt only the fraction of the UV flux that is attributed to the AGN. This model includes contributions from an inner, radiatively inefficient accretion flow, and outer, geometrically thin accretion disk, an obscured starburst and a jet. The contribution of the jet is appreciable only at the lowest radio frequencies, the starburst contributes primarily to the near-UV band, the inner, hot accretion flow dominates in the far-IR and X-ray bands, and the thin accretion disk dominates in the near-IR band. In the same spirit, we have also adopted a bolometric luminosity of 8.5×10^{41} erg s $^{-1}$ from Nemmen et al. (2006). In comparison, if we integrate the tabulated SED, we obtain a luminosity of 5.1×10^{41} erg s $^{-1}$.

NGC 3998. – To construct the SED of NGC 3998 we began from the extensive data tabulation of Ptak et al. (2004). We excluded many of the measurements presented therein because they were obtained through extremely large apertures that encompass a substantial fraction of the host galaxy (e.g., from *IRAS* observations). Since the AGN in NGC 3998 is rather bright compared to other objects in our collection, we adopted measurements through apertures as large as 3" as fair measurements of the AGN luminosity. Measurements through apertures between 3" and 15" were taken as upper limits to the AGN luminosity.

NGC 4261. – The X-ray spectrum of the AGN in NGC 4261 has been measured recently by both *Chandra* (Zezas et al. 2005) and *XMM-Newton* (Glozzi et al. 2003). Both observations yield the same spectral index and flux but significantly different equivalent hydrogen column densities (the *Chandra* spectrum yields $N_{\text{H}} = 3.7 \times 10^{20}$ cm $^{-2}$, while the *XMM-Newton* spectrum yields $N_{\text{H}} = 5.0 \times 10^{22}$ cm $^{-2}$). A UV observation with the *HST*, reported by Zirbel & Baum (1998), yields only an upper limit of $\nu L_{\nu} < 4.9 \times 10^{38}$ erg s $^{-1}$ at 2300 Å, which produces a very large dip in the SED (see Fig. 3 of Ho 1999). Neither of the column densities measured from the X-ray spectra produces a reasonable extinction correction of the UV limit; the lower value produces a negligible correction, while the higher value moves the upper limit many orders of magnitude above the monochromatic X-ray luminosity at 0.5 keV. Therefore, we infer that the AGN is indeed completely extinguished in the UV by the large equivalent hydrogen column measured from the *XMM-Newton* spectrum. Thus we derive an upper limit to the near-UV flux by assuming that $\alpha_{\text{ox}} < 1.5$, which we include in Table 3, and plot in Figure 2. Similarly, we doubt that the measurements of the nucleus of NGC 4261 in the optical band capture

the AGN. Therefore, we do not apply any extinction corrections to these measurements in Table 3 nor to the points plotted in Figure 2.

NGC 5055. – Prominent absorption lines in the UV spectrum of the nucleus of NGC 5055 suggest that hot stars dominate the light (Maoz et al. 1998). This conclusion is supported by the lack of significant UV variability and the extended morphology of the UV source (Maoz et al. 2005). Although an X-ray source with an AGN-like spectrum is detected (Flohic et al. et al. 2006), the equivalent hydrogen column density measured from the X-ray spectrum implies $E(B - V) = 0.87$, which translates into an attenuation by a factor of 100 at 2500 Å. Our conclusion is that an AGN may be present in this galaxy, but is not the source of the observed UV flux.

NGC 6500. – The UV spectrum of the nucleus of NGC 6500 (Maoz et al. 1998) has a relatively low S/N, but still shows absorption features resembling lines from hot stars. Moreover, the nuclear UV source is extended, with no clear “knot” that could be identified with the nucleus (Maoz et al. 1995; Barth et al. 1998) and no variability (Maoz et al. 2005). The X-ray spectrum (Terashima & Wilson 2003) is indicative of an obscured AGN with $E(B - V) = 0.37$, implying an attenuation of its 2500 Å flux by a factor of 7. Thus this object is very similar to NGC 5055; an AGN is probably present, but is not the source of the observed UV flux.

4. QUANTITIES DERIVED FROM THE SPECTRAL ENERGY DISTRIBUTIONS

4.1. Optical-to-X-Ray Spectral Indices, Bolometric Luminosities, and Eddington Ratios

For comparison with other types of AGNs, we have used the rest-frame flux densities at 2500 Å and 2 keV to compute the “optical-to-X-ray spectral index” (Tananbaum et al. 1979), defined as

$$\alpha_{\text{ox}} \equiv - \frac{\log [L_{\nu}(2500 \text{ \AA})/L_{\nu}(2 \text{ keV})]}{\log [\nu(2500 \text{ \AA})/\nu(2 \text{ keV})]} \\ = 1 + 0.384 \log \left[\frac{(\nu L_{\nu})_{2500 \text{ \AA}}}{(\nu L_{\nu})_{2 \text{ keV}}} \right], \quad (4)$$

under the convention that $L_{\nu} \propto \nu^{-\alpha_{\text{ox}}}$. Both the UV and X-ray flux densities were corrected for extinction, as described in §3.2, so that α_{ox} describes the shape of the intrinsic AGN spectral energy distribution. We were able to calculate the values of α_{ox} for the 9 LINERs with data available at 2500 Å and 2 keV. Another 6 objects have available data at 2500 Å but only upper limits at 2 keV; for these we were able to obtain lower limits to α_{ox} . For three objects, NGC 404, NGC 6500, and NGC 5055, we do not present the value of α_{ox} because we feel it is unreliable (see the discussion of these three objects in §3.3). In the case of NGC 404, although an AGN may contribute to observed UV and X-ray flux, there is significant contamination by hot stars, as evidenced by stellar absorption lines in the UV spectrum. In the other two objects, the UV light that we observe appears to be dominated by hot stars, with no discernible contribution from an AGN.

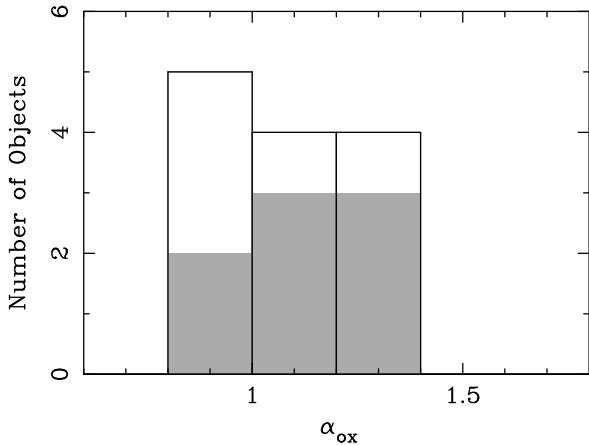


FIG. 4.— Distribution of the values of the optical-to-X-ray spectral index, α_{ox} , for 19 of the galaxies in our sample. The values were computed via equation (4). The hollow bins represent lower limits, which correspond to cases where the 2500 Å UV flux has been measured but only an upper limit to 2 keV X-ray flux is available. §3.3.

The uncertainty in α_{ox} is related to the fractional uncertainties in the X-ray and UV fluxes (as long as these are small) via $\delta\alpha_{\text{ox}} = 0.17 [(\delta f_{\text{X}}/f_{\text{X}})^2 + (\delta f_{\text{UV}}/f_{\text{UV}})^2]^{1/2}$. Typically, $\delta f_{\text{X}}/f_{\text{X}} \approx 0.1\text{--}0.2$ [dominated by uncertainties in the photon index; see footnote (a) in Table 4]⁸. The value of $\delta f_{\text{UV}}/f_{\text{UV}}$ includes a contribution from variability (typically, $\delta f_{\text{UV}}/f_{\text{UV}} \sim 0.10$ for small-amplitude variability on time scales of 1–2 years; see Table 3) and a contribution from uncertain extinction corrections (the difference between the starburst and Milky Way or Magellanic Cloud extinction laws leads to $\delta f_{\text{UV}}/f_{\text{UV}} < 0.13$ for 2/3 of our objects). Thus, under the assumption of small errors, the uncertainty in α_{ox} is 0.03. However, the above analysis does not apply if the amplitude of variability is large (it could reach a factor of a few over the course of several years; see Maoz et al. 2005) or if $E(B-V)_{\text{X}} > 0.2$ and the extinction law is uncertain. In such a case, the magnitude of the uncertainty is best illustrated by the following specific examples. If the X-ray or UV flux change by a factor of 3 between the observations in the two bands, then α_{ox} will change by 0.2. For an object such as NGC 4438 with $E(B-V)_{\text{X}} = 0.21$ the maximal difference between extinction laws yields a change in α_{ox} of 0.24, while for an object such as NGC 2681 with $E(B-V)_{\text{X}} = 0.47$, the change in α_{ox} is 0.50.

The resulting values of α_{ox} are given in Table 4 and their distribution is plotted in Figure 4. The majority of the values of α_{ox} (excluding limits) cluster between 0.92 and 1.36, while the lower limits fall between 0.55 and 1.33. It is useful to compare the values that we obtain here with those obtained by Maoz (2007) using similar data and methodology. In their sample of 12 objects (excluding NGC 404) (Maoz 2007) find a range of α_{ox} of 0.92–1.34, very similar to ours. Moreover, comparing the values of α_{ox} in five individual objects that are common between the two papers, we find that in four cases they agree within 0.16 and in the case of NGC 4594 the values disagree by 0.31. We attribute the differences in the values of α_{ox} to the following differences in the analysis: (a) Maoz (2007) did not apply corrections for intrinsic extinction in the

⁸ The uncertainty on f_{X} should also have contribution from variability, which we are unable to estimate because of the lack of systematic monitoring data.

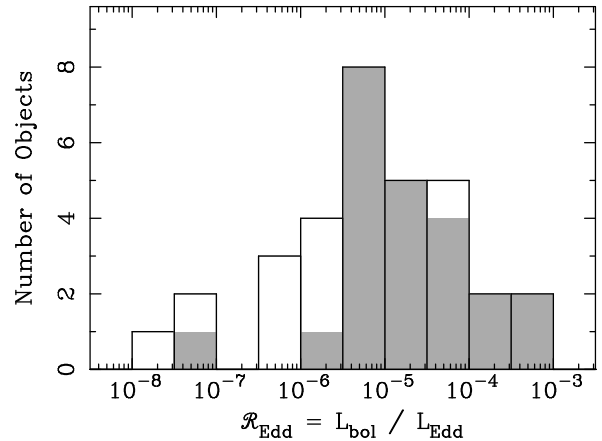


FIG. 5.— Distribution Eddington ratios for the AGNs in our sample. These were computed via equation (5), with bolometric luminosities estimated as described in §3 of the text. The hollow histogram bins represent upper limits. The galaxies NGC 266, NGC 3507, and NGC 4438 are not included because their black hole masses are not available.

vicinity of the AGN, while we did, and (b) Maoz (2007) used a fixed value of 1.8 for the X-ray photon index to obtain the 2 keV monochromatic luminosity, while we used the specific value of the photon index measured from each X-ray spectrum. Thus we conclude that the true range of values is likely between 0.9–1.4. We take 1.5 to be a very generous upper limit to the value of α_{ox} and use it to derive upper limits to the 2500 Å monochromatic luminosity of the objects for which no such measurement or limit is available (see §3.1).

We have computed the bolometric luminosities of a set of “calibration objects” with well-sampled SEDs by integrating the SEDs directly (neglecting upper limits). These objects are NGC 3031, NGC 3998, NGC 4374, NGC 4486, NGC 4579, and NGC 4594. For another object, NGC 1097, we adopted the bolometric luminosity derived from a model for the SED by Nemmen et al. (2006). To integrate an SEDs we assumed that pairs of neighboring points defined a power law, computed the integral for each segment analytically, and summed the luminosities of individual segments. Using this small subset of objects, we estimated the “bolometric correction,” $\kappa_{2-10\text{ keV}}$, such that $L_{\text{bol}} = \kappa_{2-10\text{ keV}} L_{2-10\text{ keV}}$. We found that the values of $\kappa_{2-10\text{ keV}}$ in this small subset span a wide range, from 6 to 143, with a geometric mean of 33, a median of 52, and an average of 51. This range is comparable to the range found in Seyfert galaxies and quasars by Vasudevan & Fabian (2007). Thus, we adopted $\kappa_{2-10\text{ keV}} = 50$ and used it to obtain the bolometric luminosity of the remaining objects in our sample from their 2–10 keV X-ray luminosities. We list these bolometric luminosities in Table 4.

Using the bolometric luminosities estimated above, we computed the Eddington ratios of the AGNs in our sample (the ratio of the bolometric luminosity of the AGN and the Eddington luminosity) as follows:

$$\mathcal{R}_{\text{Edd}} \equiv L_{\text{bol}}/L_{\text{Edd}} = 7.7 \times 10^{-7} L_{40} M_8^{-1}$$

$$\text{or } \log \mathcal{R}_{\text{Edd}} = -6.11 + \log L_{40} - \log M_8, \quad (5)$$

where $L_{\text{bol}} = 10^{40} L_{40} \text{ erg s}^{-1}$ is the bolometric luminosity, $L_{\text{Edd}} = 1.3 \times 10^{38} (M_{\text{BH}}/M_{\odot}) \text{ erg s}^{-1}$, is the Eddington luminosity, and $M_{\text{BH}} = 10^8 M_8 M_{\odot}$ is the black hole mass reported in Table 1. The resulting values of \mathcal{R}_{Edd} are included in Table 4; they span the range $-7.8 < \log \mathcal{R}_{\text{Edd}} < -3.4$ for the AGNs in our sample that were *detected* in the X-ray band.

The distribution of Eddington ratios is shown graphically in Figure 5.

Estimating the bolometric luminosity by scaling the 2–10 keV luminosity is subject to a number of caveats. These caveats also apply to the estimates of the Eddington ratio. First, it is not known whether there is a single, universal value of the bolometric correction. On theoretical grounds, we would expect the shapes of the SEDs of low-Eddington ratio AGNs, hence the bolometric corrections, to depend on the black hole mass and accretion rate (see, for example, Ball et al. 2001, and references therein). The objects in our calibration set span a relatively narrow range in luminosity, mass, and Eddington ratio [$41.3 < \log(L_{\text{bol}}/\text{erg s}^{-1}) < 43.1$, $7.8 < \log(M_{\text{BH}}/M_{\odot}) < 9.5$, $-3.8 < \log \mathcal{R}_{\text{Edd}} < -5.3$], but we have applied this correction to objects with a much wider range in these properties, namely down to $\log(M_{\text{BH}}/M_{\odot}) = 5.3$ and $\log \mathcal{R}_{\text{Edd}} = -7.8$. We have checked whether there is any correlation between $\kappa_{2-10\text{keV}}$ or α_{ox} , and the mass, luminosity, or Eddington ratio in our calibration set but found none. Second, the values of $\kappa_{2-10\text{keV}}$ within our calibration set span a rather wide range even though they were derived from objects with a narrow range of properties. This suggests that either (a) there are systematic errors in the measured bolometric luminosities, or (b) there is a wide diversity in the SEDs. Systematic errors could arise from our interpolating over broad but sparsely-sampled frequency windows (especially in the far-IR) or from contamination by light from the host galaxy (especially in the near-IR). In conclusion, we note that the values of the bolometric luminosity and the Eddington ratio that we report in Table 4 should be regarded with caution; we estimate rough uncertainties on these quantities of a factor of 5 in either direction.

In an effort to assess any relation between LINER class and AGN luminosity, which may reveal selection effects or other biases in this sample, we plot in Figure 6 the bolometric luminosities we have derived against the black hole mass. In this figure we use different symbols to denote different LINER classes (L1, L2, and T2 or T2/L2). An inspection of this figure shows that L2 and T2 LINERs span the entire range of luminosities of the sample, although L2 objects are concentrated at higher luminosities. This is not a surprise because more luminous objects, which also appear brighter in the narrow range of distances of this sample, are more attractive targets for pointed X-ray observations. L1 LINERs are found preferentially at high luminosities, which we attribute to a selection effect of the optical spectroscopic survey that detected them (Ho et al. 1997c). More specifically, the luminosity of their broad lines, which determines how easily they can be detected, depends directly on the luminosity of the AGN.

4.2. The Average Spectral Energy Distribution and Its Properties

For the sake of completeness, we have also produced an average SED using the following procedure. First, all individual SEDs were normalized (arbitrarily) to an integrated 2–10 keV X-ray luminosity of $10^{40} \text{ erg s}^{-1}$. Because of this normalization scheme, we had to exclude 11 AGNs for which we only have X-ray upper limits. After normalization, the available measurements were grouped into frequency bins, neglecting upper limits as well as the SEDs of NGC 404, NGC 5055, and NGC 6500, which appear to be significantly contaminated or dominated by starlight (see §3.3). Finally, we computed the geometric mean in each bin by averaging the logarithm of the

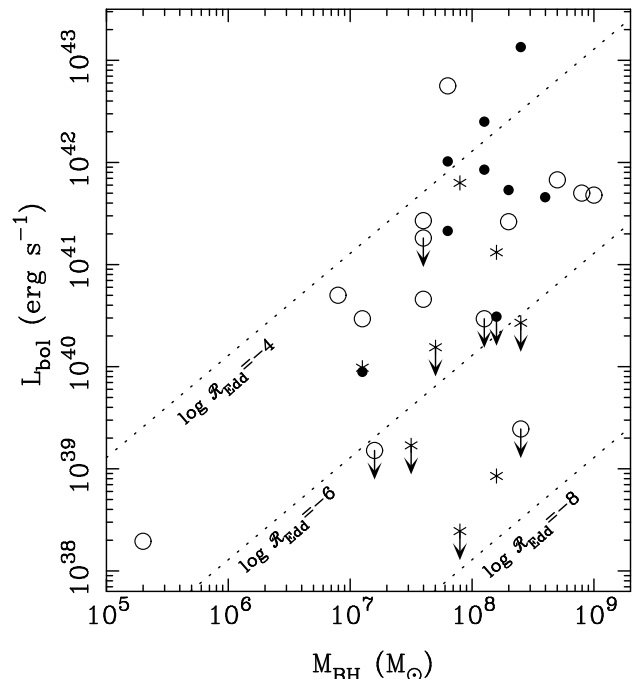


FIG. 6.— Bolometric luminosities (see §4.1) plotted against black hole mass. The galaxies NGC 266, NGC 3507, and NGC 4438 are not included because their black hole masses are not available. Arrows denote upper limits on the bolometric luminosity, while different symbols represent different LINER classes: L1 objects are plotted as filled circles, L2 objects as open circles, and T2 and two L2/T2 objects as asterisks. For reference, diagonal dotted lines indicate the locus of constant Eddington ratio for $\log \mathcal{R}_{\text{Edd}} = -4, -6, -8$ (from top to bottom).

luminosity, $\langle \log(\nu L_{\nu}) \rangle$). The geometric mean is preferable to the simple mean because it minimizes the effect of extreme outliers. We have found that the geometric mean is very similar to the median in each frequency bin. For frequency bins between 0.1 and 1 μm we have computed the geometric mean both before and after applying extinction corrections. The results are tabulated in Table 5, which also includes the definition of the frequency bins used, the standard deviation of $\log(\nu L_{\nu})$, and the number of measurements in each frequency bin. The X-ray photon index in the (geometric) mean SED is 1.85 and the value of α_{ox} is 1.24. In comparison, the subset of objects with a measured value of α_{ox} have a median X-ray photon index of 1.90 and a median α_{ox} of 1.28.

The mean SED is plotted in Figure 7 where we also overplot the mean SEDs of radio-loud and radio-quiet quasars (Elvis et al. 1994), after normalizing them to the same X-ray luminosity, for comparison. It is noteworthy that the mean LINER SED has an X-ray band slope similar to that of radio-quiet quasars but a relative radio luminosity and slope similar to that of radio-loud quasars. In the UV band, around 1 Ry, the luminosity in the quasar SEDs is somewhat higher than in the mean LINER SED, although there is agreement within the 1- σ dispersion limits. It is also interesting to compare the mean LINER SED derived here with the LINER SEDs presented by Ho (1999, see his Fig. 8). The near-UV luminosity in our SED appears to be higher (relative to the X-ray luminosity) than that of the Ho (1999) SEDs. This is also apparent from a comparison of the values of α_{ox} determined by Ho (1999) and by us. We attribute this difference to newer measurements in both the UV and X-ray bands. Measurements in the X-ray band with *Chandra* have isolated the X-ray emission from the AGN and reduced the contamination from

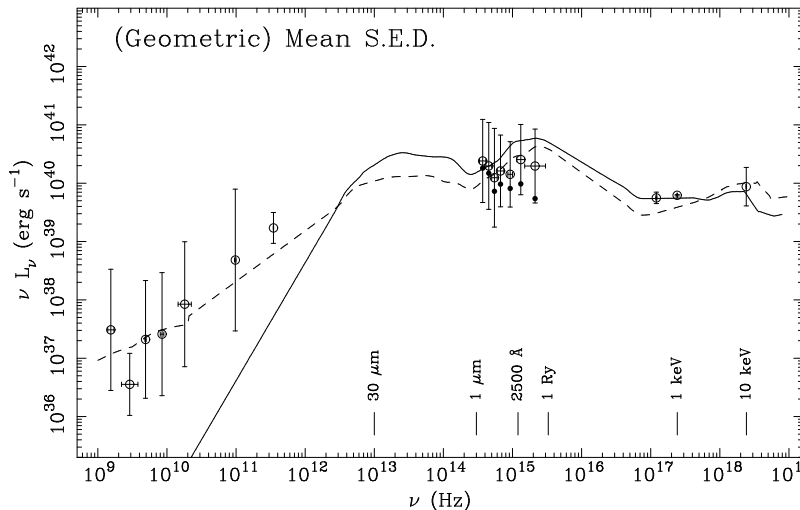


FIG. 7.— The geometric mean SED of the LINERs in our sample. The open circles represent the average after extinction corrections, while the filled circles show the average before any extinction corrections are applied (in the range 0.1–1 μm only). The vertical error bars indicate the standard deviation in $\log(\nu L_\nu)$. The horizontal error bars represent the frequency bands within which measurements were averaged. Overplotted are the average SEDs of radio-quiet and radio-loud quasars (solid and dashed lines respectively; from Elvis et al. 1994). Additional details can be found in §4.2 of the text and in Table 5.

TABLE 5
AVERAGE SPECTRAL ENERGY DISTRIBUTION^a

| Band Limits ^b | | Number of Points ^c | $\log\langle\nu\rangle$ | Corrected ^d | | Uncorrected ^e |
|--------------------------|-----------------------|----------------------------------|-------------------------|---------------------------------|-----------------------------|--|
| ν_{\min} (1) | ν_{\max} (2) | | | $\langle\log(\nu L_\nu)\rangle$ | $\sigma[\log(\nu L_\nu)]^f$ | $\langle\log(\nu L_\nu)\rangle$ (7) |
| 1.390×10^9 | 1.710×10^9 | 10 | 9.19 | 37.49 | 1.04 | |
| 2.200×10^9 | 3.800×10^9 | 4 | 9.48 | 36.55 | 0.53 | |
| 4.800×10^9 | 5.000×10^9 | 14 | 9.69 | 37.32 | 1.01 | |
| 8.000×10^9 | 9.000×10^9 | 7 | 9.93 | 37.41 | 1.05 | |
| 1.450×10^{10} | 2.250×10^{10} | 15 | 10.27 | 37.93 | 1.07 | |
| 9.500×10^{10} | 1.000×10^{11} | 10 | 10.99 | 38.68 | 1.21 | |
| 3.450×10^{11} | 3.500×10^{11} | 3 | 11.54 | 39.23 | 0.26 | |
| 3.333×10^{14} | 4.110×10^{14} | 10 | 14.57 | 40.38 | 0.71 | 40.26 |
| 4.110×10^{14} | 5.000×10^{14} | 5 | 14.66 | 40.30 | 0.74 | 40.17 |
| 5.000×10^{14} | 6.000×10^{14} | 8 | 14.74 | 40.09 | 0.85 | 39.86 |
| 6.000×10^{14} | 7.500×10^{14} | 4 | 14.83 | 40.21 | 0.62 | 39.98 |
| 8.571×10^{14} | 1.000×10^{15} | 8 | 14.97 | 40.15 | 0.56 | 39.91 |
| 1.154×10^{15} | 1.500×10^{15} | 14 | 15.12 | 40.40 | 0.60 | 39.99 |
| 1.500×10^{15} | 3.000×10^{15} | 8 | 15.35 | 40.29 | 0.63 | 39.74 |
| 1.182×10^{17} | 1.231×10^{17} | 21 | 17.08 | 39.75 | 0.10 | |
| 2.389×10^{17} | 2.437×10^{17} | 21 | 17.38 | 39.79 | 0.01 | |
| 2.389×10^{18} | 2.437×10^{18} | 21 | 18.38 | 39.94 | 0.33 | |

^a Frequencies are measured in Hz and monochromatic luminosities (νL_ν) are measured in erg s^{-1} .

^b The limits of the frequency bands used to group the data points from individual SEDs.

^c The number of data points in each frequency bin.

^d Average values of $\log(\nu L_\nu)$ and its standard deviation *after* correcting for extinction using the Seaton (1979) law.

^e Average values of $\log(\nu L_\nu)$ from 0.1 to 1 μm *without* extinction corrections.

^f The standard deviation in the *corrected* values of $\log(\nu L_\nu)$ (omitted when a bin contains only a single data point).

circumnuclear sources (e.g., Flohic et al. et al. 2006), thus increasing the contrast between the UV and X-ray luminosity.

We emphasize that interpretation or use of the average SED requires care for the following reasons. First and foremost, the average SED includes contributions from objects with a wide range of Eddington ratios, with the caveats discussed at the end of §4.1. We do note, however, that the dominant contribution is from objects with $-5.4 < \log \mathcal{R}_{\text{Edd}} < -4.0$ (see Fig. 5). Second, not all objects contribute to all frequency bins of the average SED. Each bin includes a different mix of objects, with the exception of the X-ray bins, where by

construction all objects contribute. Third, in frequency bins containing a small number of measurements, the standard deviation is depressed. In spite of these caveats, however, one can use more specific filters for the data tabulated here in order to construct an average SED that is suitable for testing accretion flow models.

We thank the referee, D. Maoz for many helpful comments and E. C. Moran for a careful and critical reading of the manuscript. This work was partially supported by the Na-

tional Aeronautics and Space Administration through *Chandra* award number AR4-5010A issued by the *Chandra* X-Ray Observatory Center, which is operated by the Smithsonian Astrophysical Observatory for and on behalf of the National Aeronautics and Space Administration under contract

NAS8-03060. This research has made use of the NASA/IPAC Extragalactic Database (NED) which is operated by the Jet Propulsion Laboratory, California Institute of Technology, under contract with the National Aeronautics and Space Administration.

REFERENCES

- Anders, E. & Ebihara, M. 1982, *Geochim. Cosmochim. Acta*, 46, 2363
 Ball, G. H., Narayan, R., & Quataert, E. 2001, *ApJ*, 552, 221
 Barth, A. J., Ho, L. C., Filippenko, A. V., & Sargent, W. L. W. 1998, *ApJ*, 496, 133
 Barth, A. J., Ho, L. C., & Sargent, W. L. W. 2002, *AJ*, 124, 2607
 Barth, A. J., & Shields, J. C. 2000, *PASP*, 112, 753
 Becker, R. H., White, R. L., & Helfand, D. J. 1995, *ApJ*, 450, 559
 Binette, L., Magris, C. G., Stasinska, G., & Bruzual, A. G. 1994, *A&A*, 292, 13
 Bouchet, P., Lequeux, J., Maurice, E., Prevot, L., & Prevot-Burnichon, M. L., 1985, *A&A*, 149, 330
 Bower, G. A. et al. 1998, *ApJ*, 492, 111
 Bower, G. A., Wilson, A. S., Heckman, T. M., Magorrian, J., Gebhardt, K., Richstone, D. O., Peterson, B. M., & Green, R. F. 2000, *Bulletin of the American Astronomical Society*, 32, 1566
 Calzetti, D., Kinney, A. L., & Storchi-Bergmann, T. 1994, *ApJ*, 429, 582
 Cappi, M. et al. 2006, *A&A*, 446, 459
 Cardelli, J. A., Clayton, G. C., & Mathis, J. S. 1989, *ApJ*, 345, 245
 Chiaberge, M., Capetti, A., & Celotti, A. 1999, *A&A*, 349, 77
 Chiaberge, M., Capetti, A., & Macchetto, F. D. 2005, *ApJ*, 625, 716
 Ciardullo, R., Feldmeier, J. J., Jacoby, G. H., Kuzio de Naray, R., Laychak, M. B., & Durrell, P. R. 2002, *ApJ*, 577, 31
 Condon, J. J., Cotton, W. D., Greisen, E. W., Yin, Q. F., Perley, R. A., Taylor, G. B., & Broderick, J. J. 1998, *AJ*, 115, 1693
 Devereux, N., Ford, H., Tsvetanov, Z., & Jacoby, G. 2003, *AJ*, 125, 1226
 de Francesco, G., Capetti, A., & Marconi, A. 2006, *A&A*, 460, 439
 Doi, A., Kamenno, S., & Inoue, M. 2005a, *MNRAS*, 360, 119
 Doi, A., Kamenno, S., Kohno, K., Nakanishi, K., & Inoue, M. 2005b, *MNRAS*, 363, 692
 Dopita, M. A., Koratkar, A. P., Evans, I. N., Allen, M., Bicknell, G. V., Sutherland, R. S., Hawley, J. F., & Sadler, E. 1996, in *The physics of Liners in view of recent observations*. ASP Conference Series, Vol. 103, ed. Eracleous, M., Koratkar, A., Leitherer, C., & Ho, L., p.44
 Dudik, R. P., Satyapal, S., Gliozzi, M., & Sambruna, R. M. 2005, *ApJ*, 620, 113
 Dudik, R. P., Satyapal, S., & Marcu, D. 2009, *ApJ*, 691, 1501
 Elvis, M., Wilkes, B. J., McDowell, J. C., Green, R. F., Bechtold, J., Willner, S. P., Oey, M. S., Polomski, E., & Cutri, R. 1994, *ApJS*, 95, 1
 Eracleous, M., Hwang, J. A., & Flohic, H. M. L. G. 2009, *ApJ*, submitted (paper II)
 Eracleous, M., Shields, J. C., Chartas, G., & Moran, E. C. 2002, *ApJ*, 565, 108
 Ferland, G. J. & Netzer, H. 1983, *ApJ*, 264, 105
 Ferrarese, L., Ford, H. C., & Jaffe, W. 1996, *ApJ*, 470, 444
 Ferrarese, L., & Merritt, D. 2000, *ApJ*, 539, L9
 Filippenko, A. V., & Terlevich, R. 1992, *ApJ*, 397, L79
 Filho, M. E., Fraternali, F., Markoff, S., Nagar, N. M., Barthel, P. D., Ho, L. C., & Yuan, F. 2004, *A&A*, 418, 429
 Flohic, H. M. L. G., Eracleous, M., Chartas, G., Shields, J. C., & Moran, E. C. 2006, *ApJ*, 647, 140
 Freedman, W. L. et al. 1994, *ApJ*, 427, 628
 Freedman, W. L. et al. 2001, *ApJ*, 553, 47
 Gavazzi, G., Boselli, A., Scodreggio, M., Pierini, D., & Belsole, E. 2009, *MNRAS*, 304, 595
 Gebhardt, K., et al. 2000, *ApJ*, 539, L13
 González-Martín, O., Masegosa, J., Márquez, I., Guerrero, M. A., & Dultzin-Hacyan, D. 2006, *A&A*, 460, 45
 Gliozzi, M., Sambruna, R. M., & Brandt, W. N. 2003, *A&A*, 408, 949
 Halpern, J. P. & Steiner, J. E. 1983, *ApJ*, 269, L37
 Heckman, T. M. 1980, *A&A*, 87, 152
 Herrmann, K. A., Ciardullo, R., Feldmeier, J. J., & Vinciguerra, M. 2008, *ApJ*, 683, 630
 Ho, L. C. 1999, *ApJ*, 516, 672
 Ho, L. C. 2008, *ARA&A*, 46, 475
 Ho, L. C., Filippenko, A. V., & Sargent, W. L. W. 1997, *ApJ*, 487, 568
 Ho, L. C., Filippenko, A. V., & Sargent, W. L. W. 1997, *ApJS*, 112, 315
 Ho, L. C., Filippenko, A. V., Sargent, W. L. W., & Peng, C. Y. 1997, *ApJS*, 112, 391
 Ho, L. C. et al. 2001, *ApJ*, 549, L61
 Jensen, J. B., Tonry, J. L., Barris, B. J., Thompson, R. I., Liu, M. C., Rieke, M. J., Ajhar, E. A., & Blakeslee, J. P. 2003, *ApJ*, 583, 712
 Karachetsev, I. D. et al. 2002, *A&A*, 389, 812
 Karachetsev, I. D. et al. 2003, *A&A*, 398, 467
 Karachetsev, I. D., Karachetseva, V. E., Huchtmeier, W. K., & Makarov, D. I. 2004, *AJ*, 127, 2031
 Kauffmann, G. et al. 2003, *MNRAS*, 346, 1055
 Kewley, L., Dopita, M., Sutherland, R., Heissler, C., & Trevena, J. 2001, *ApJ*, 556, 121
 Kewley, L. J., Groves, B., Kauffmann, G., & Heckman, T. 2006, *MNRAS*, 372, 961
 Kormendy, J., et al. 1996, *ApJ*, 473, L91
 Korneef, J. & Code, A. 1981, *ApJ*, 247, 860
 Lewis, K. T. & Eracleous, M. 2006, *ApJ*, 642, 711
 Macchetto, F., Marconi, A., Axon, D. J., Capetti, A., Sparks, W., & Crane, P. 1997, *ApJ*, 489, 579
 Maoz, D. 2007, *MNRAS*, 377, 1696
 Maoz, D., Filippenko, A. V., Ho, L. C., Rix, H.-W., Bahcall, J. N., Schneider, D. P., & Macchetto, F. D., 1995, *ApJ*, 440, 91
 Maoz, D., Filippenko, A. V., Ho, L. C., Macchetto, F. D., Rix, H.-W., & Schneider, D. P. 1996, *ApJS*, 107, 205
 Maoz, D., Koratkar, A., Shields, J. C., Ho, L. C., Filippenko, A. V. & Sternberg, A. 1998, *AJ*, 116, 55
 Maoz, D., Nagar, N. M., Falcke, H., & Wilson, A. S. 2005, *ApJ*, 625, 699
 Morrison, R. & McCammon, D. 1983, *ApJ*, 270, 119
 Nagar, N. M., Falcke, H., Wilson, A. S., & Ho, L. C. 2000, *ApJ*, 542, 186
 Nagar, N. M., Falcke, H., & Wilson, A. S. 2005, *A&A*, 435, 531
 Nandra, K., George, I. M., Mushotzky, R. F., Turner, T. J., & Yaqoob, T. 1997, *ApJ*, 477, 602
 Nemmen, R. S., Storchi-Bergmann, T., Yuan, F., Eracleous, M., & Wilson, A. S. 2006, *ApJ*, 643, 652
 Pellegri, S., Baldi, A., Fabbiano, G., & Kim, D.-W. 2003, *ApJ*, 597, 175
 Phillips, M. M., Jenkins, C. R., Dopita, M. A., Sadler, E. M., & Binette, L. 1986, *AJ*, 91, 1062
 Phillips, M. M., Pagel, B. E. J., Edmunds, M. G. & Diaz, A. 1984, *MNRAS*, 210, 701
 Prieto, M. A., Maciejewski, W., & Reunanen, J. 2005, *AJ*, 130, 1472
 Schlegel, D. J., Finkbeiner, D. P., & Davis, M. 1998, *ApJ*, 500, 525
 Predhřl, P. & Schmitt, J. H. M. M. 1995, *A&A*, 293, 889
 Ptak, A., Terashima, Y., Ho, L. C., & Quataert, E. 2004, *ApJ*, 606, 173
 Satyapal, S., Sambruna, R. M., & Dudik, R. P., 2004, *A&A*, 414, 825
 Seaton, M. J. 1979, *MNRAS*, 187, 83P
 Shields, J. C. 1992, *ApJ*, 399, L27
 Steffen, A. T., Strateva, I., Brandt, W. N., Alexander, D. M., Koekemoer, A. M., Lehmer, B. D., Schneider, D. P., Vignali, C. 2006, *AJ*, 131, 2826
 Storchi-Bergmann, T., Nemmen, R. S., Spinelli, P. F., Eracleous, M., Wilson, A. S., Filippenko, A. V., & Livio, M. 2005, *ApJ*, 624, L13
 Strateva, I. V., Brandt, W. N., Schneider, D. P., Vanden Berk, D. G., & Vignali, C. 2005, *AJ*, 130, 387
 Tananbaum, H., et al. 1979, *ApJ*, 234, L9
 Terashima, Y. & Wilson, A. S. 2003, *ApJ*, 583, 145
 Tonry, J. L., Dressler, A., Blakeslee, J. P., Ajhar, E. A., Fletcher, A. B., Luppino, G. A., Metzger, M. R., & Moore, C. B. 2001, *ApJ*, 546, 681
 Terlevich, R., & Melnick, J. 1985, *MNRAS*, 213, 841
 Tremaine, S., et al. 2002, *ApJ*, 574, 740
 Tully, R. B. 1988, *Nearby Galaxies Catalog* (Cambridge: Cambridge University Press)
 Vasudevan, R. V. & Fabian, A. C. 2007, *MNRAS*, 381, 1235
 Wilson, A. S. & Yang, Y. 2002, *ApJ*, 568, 133
 Zezas, A., Birkinshaw, M., Worrall, D. M., Peters, A., & Fabbiano, G. 2005, *ApJ*, 627, 711-720
 Zirbel, E. L., & Baum, S. A. 1998, *ApJS*, 114, 177